



Hydroelastic analysis of underwater rotating elastic marine propellers by using a coupled BEM-FEM algorithm

Jiasheng Li^{a,b}, Yegao Qu^a, Hongxing Hua^{a,b,*}

^a State Key Laboratory of Mechanical System and Vibration, Shanghai Jiao Tong University, Shanghai, 200240, PR China

^b Collaborative Innovation Center for Advanced Ship and Deep-Sea Exploration (CISSE), Shanghai Jiao Tong University, Shanghai, 200240, PR China

ARTICLE INFO

Keywords:

Fluid-structure interaction
Hydroelastic responses
Propeller
Added mass
Added damping

ABSTRACT

This paper focuses on the development of a numerical method for analyzing the added mass and damping of a rotating elastic marine propeller. Three-dimensional panel methods in frequency domain combined with the finite element method were employed to study the strongly coupled fluid-structure interactions of the propeller. In order to overcome the computational efficiency problem due to the asymmetric added matrices of the fluid, a mode superposition method in conjunction with Wilson-θ method was employed for calculating the structural responses of the propeller. The validity of the proposed numerical method was confirmed by comparing the present results with experimental data available in the literature and those numerical solutions computed using commercial packages ANSYS and Virtual.Lab Acoustics. The effects of the excitation frequency, inflow velocity, material parameter of propeller and the advance ratio on the added mass and damping of rotating elastic propellers were examined. The results showed that stationary flow may be sufficient for analyzing the wet modes of the propeller at a relatively high excitation frequency, and the non-penetration boundary conditions should be imposed on the deformed blade surface rather than the undeformed surface in the case of relatively lower-frequency excitations. In addition, if the inflow velocity is relatively large, the added damping due to the fluid can significantly affect the unsteady performance of the propeller.

1. Introduction

The knowledge of the vibrational properties of propellers is of great importance for successful design of modern marine propellers, especially for light weight and flexible propellers. As is well-known, the presence of the water around a vibrating propeller may change the dynamic characteristics of the propeller significantly. Generally speaking, the hydrodynamic forces of the fluid acting on a propeller can be represented by the added mass and damping due to the fluid, which are proportional to the structural responses (acceleration and velocity) of the propeller. In certain cases, the added mass and damping due to the fluid can be of the same order of magnitude, or even higher than the structural mass and damping of the solid. Thus, for many marine propellers, the knowledge of the effects of the added mass and damping on the structural behaviors of the propeller is of critical importance for predicting the vibration characteristics of the propulsion system.

In practice, a marine propeller may vibrate in various manners. However, the most important modes of the vibrations of the propeller fall into two categories, i.e., (A) vibrations of the whole propeller, such as

surge, sway, heave, roll, pitch and yaw vibration modes, (B) local vibrations of the blades (as distinct from the vibration of the whole propeller). Since the wet modes of the propeller vibrations are different, there will be different effects of the hydrodynamic mass and damping due to the fluid.

Several methods have been proposed in the literature to study the effects of the added mass and damping on the vibrations of marine propellers. Lin and Tsai (2008) examined the free vibration of an underwater composite propeller blade by using the finite element method combined with the panel method. The added mass effect was considered, and the natural frequencies of the blade in wet condition were found to be much lower than those of the blade in dry condition. However, the mode shapes of the blade were found to be almost the same regardless of the blade in wet or dry conditions. Yari and Ghassemi (2016) calculated the added mass coefficients for whole propeller vibrations based on the boundary element method. The results showed that the diameter, expanded area ratio, and the thickness of the propeller have significant influence on the added mass coefficients. MacPherson et al. (2007) proposed a semi-empirical formula to predict the axial water added mass

* Corresponding author. State Key Laboratory of Mechanical System and Vibration, Shanghai Jiao Tong University, Shanghai, 200240, PR China.
E-mail address: hhx@sjtu.edu.cn (H. Hua).

and the torsional water moment due to the vibration of the propeller. However, their formulas were based on experimental data of the Wageningen B-series and the KCA series, which may limit the application of their methods. Gaschler and Abdel-Maksoud (2014) obtained the added mass and damping coefficients of heaving motion in 'A' kind of vibration for a marine propeller by using a 3-D panel method. Both non-cavitating and cavitating conditions were investigated, and the results revealed that unsteady sheet cavitation seems to have a negligible influence on the magnitudes of the hydrodynamic mass and damping coefficients. Martio et al. (2015) calculated the added mass and damping coefficients in 'A' kind of vibration by prescribing sinusoidal translational and rotational motions for a propeller. For determining the effect of the viscosity on the vibrational coefficients, URANS computations were considered in their study. The viscous effects were found to be significant for some coefficients. Mao and Young (2016) applied a 3-D curved lifting line model coupled with a 2-D unsteady thin foil theory to study the added mass and damping coefficients in 'A' kind of vibration. It was found that the skew can affect the coupled motions with the sway, heave, pitch, and yaw components of the added mass and damping matrices, while the influence of the skew on the surge and roll components is negligible. The above review indicates that very limited research effort has been devoted to the analysis of hydrodynamic mass and damping for the 'B' kind of vibration. This motivates the present work.

The objective of the present paper is to develop a highly efficient numerical method to analyze the added mass and damping due to a rotating propeller immersed in water. Regarding the fluid-structure interactions of the propeller, the kinematic boundary conditions on the blade surface were derived by considering the non-penetration conditions. The governing equations of the propeller and the fluid were established, and the added-mass and-damping matrices due to the fluid-structure interaction were obtained in a rigorous way. The finite element method combined with a frequency-dependent panel method was used to formulate the structure model and the added mass and damping matrices due to fluid. Subsequently, a modal reduction technique combined with Wilson-θ method was employed to calculate the structural responses of the propeller, which overcomes the low numerical efficiency due to the asymmetric added matrices of the fluid. The present results were compared with experimental data available in the literature and those numerical solutions obtained from commercial software. Very good agreement was achieved. The effects of the added mass and damping on the unsteady performance of the propeller were investigated.

2. Mathematical model

2.1. Governing equations of propeller blade

For the sake of brevity, a single propeller blade with a unit force applied at the end of the blade is considered. A Cartesian o-xyz coordinate system rotating and advancing with the propeller blade is introduced to describe the motion of the blade. The generator line of the blade is coincident with the positive y-axis, and the x-axis is in parallel with the shaft center line, positive afterward, as shown in Fig. 1. The hub is not considered, and the blade is assumed to be fixed at its root. The blade is considered to be made of an isotropic, homogeneous and linear elastic material. The material properties of the blade are given as: Young's modulus E , Poisson's ratio ν , and density ρ . Due to the irregularity of the geometrical configuration of the blade, three-dimensional linear isoparametric elements are employed to spatially discretize the propeller blade. Each blade element has eight nodes and a total of 24 degrees of freedom.

Using the Lagrange's method, the discretized equations of motion for the elastic blade can be written as:

$$\mathbf{M}\ddot{\mathbf{u}} + (\mathbf{C}_\Omega + \mathbf{C})\dot{\mathbf{u}} + (\mathbf{K}_\Omega + \mathbf{K})\mathbf{u} = \mathbf{F}_\Omega + \mathbf{F} + \mathbf{F}_w \quad (1)$$

where $\ddot{\mathbf{u}}, \dot{\mathbf{u}}$ and \mathbf{u} are the vectors containing the nodal acceleration,

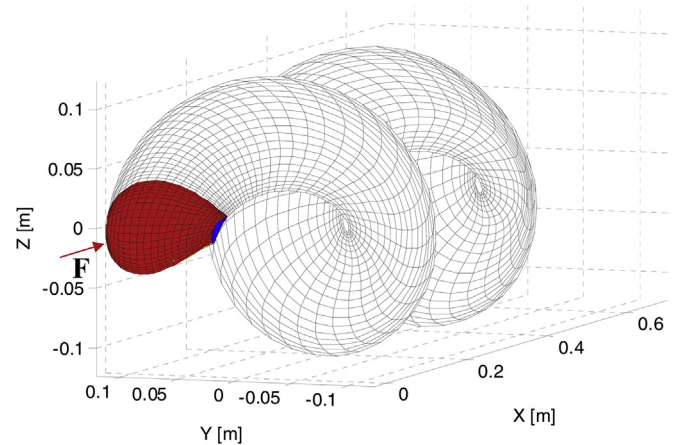


Fig. 1. The propeller-fixed coordinate system which rotates with the propeller (X, Y, Z) coordinate system is shown.

velocity, and displacement components of the blade, respectively; \mathbf{M} and \mathbf{K} are the global mass and stiffness matrices assembled by the element matrices \mathbf{M}^e and \mathbf{K}^e , defined as: $\mathbf{M}^e = \iiint_{V_e} \rho_s \mathbf{N}^T \mathbf{N} dV$ and $\mathbf{K}^e = \iiint_{V_e} \mathbf{B}^T \mathbf{D}_s \mathbf{B} dV$, where \mathbf{N} is the shape function matrix, \mathbf{B} is the strain-displacement matrix and \mathbf{D}_s is the material constitutive matrix of each element. The Rayleigh damping model is considered here for taking into account the structural damping of the propeller. In doing so, the damping of the propeller can be represented by a global damping matrix \mathbf{C} , given as $\mathbf{C} = \alpha \mathbf{M} + \beta \mathbf{K}$, where α and β are two pre-assigned constants. In Eq. (1), $\mathbf{C}_\Omega \dot{\mathbf{u}}, \mathbf{K}_\Omega \mathbf{u}$ and \mathbf{F}_Ω are the equivalent force vectors due to the centrifugal and Coriolis forces, which are assumed to be negligible when the rotating speed of the blade is small. \mathbf{F} is the unit force vector due to the structural forces, and \mathbf{F}_w is the hydrodynamic force vector due to the fluid-structural interaction.

2.2. Governing equations of fluid

The flowing fluid surrounding the propeller is assumed to be incompressible, inviscid and irrotational. A panel method is employed to determine the hydrodynamic force vector \mathbf{F}_w . The total velocity \mathbf{V}_{total} of the fluid can be expressed in the sum of a uniform inflow velocity \mathbf{V}_0 and a disturbed velocity due to a perturbation potential ϕ , given as:

$$\mathbf{V}_{total} = \mathbf{V}_0 + \nabla \phi \quad (2)$$

where ϕ is the perturbation velocity potential corresponding to the propeller-induced flow field. ∇ is the gradient operator.

According to the potential flow theory and the kinematic boundary conditions of the fluid on the blade surface, the propeller-induced perturbation potential ϕ can be written as:

$$\nabla^2 \phi = 0, \text{ in fluid domain } \Omega \quad (3)$$

$$-\frac{\partial \phi}{\partial \mathbf{n}} = \mathbf{V}_0 \cdot \mathbf{n} - \frac{\partial \delta}{\partial t} \cdot \mathbf{n} + ((\delta \cdot \nabla) \mathbf{V}_0) \cdot \mathbf{n}, \text{ on blade surface } \Gamma \quad (4)$$

$$\Delta \phi_w(\mathbf{R}_{wake}, t) = \Delta \phi(\mathbf{R}_{re}, t - t'), \text{ Morino-Kutta condition} \quad (5)$$

where \mathbf{n} is the outward unit normal vector. δ is the displacement vector for the nodal points on the blade surface. \mathbf{V}_0 is the velocity of the incoming flow. $\Delta \phi_w(\mathbf{R}_{wake}, t)$ represents the potential jump across the wake sheets. $\Delta \phi(\mathbf{R}_{re}, t - t')$ is the potential jump across the blade surface at the trailing edge, which is equal to the potential at the upper side (suction side) subtracting that at the lower side (pressure side). t' is the time required for the fluid traveling from the blade trailing edge \mathbf{R}_{re} to the wake point \mathbf{R}_{wake} along the wake surface. The kinematic boundary condition defined in Eq.

(4) requires the flow to be tangent to the deformed blade surface, which forms a Neumann-type boundary condition. For more details about the Morino Kutta condition defined in Eq. (5), the reader is referred to Morino and Kuo (1974).

Small deformation of the propeller is considered in this work. The propeller-induced perturbation potential ϕ can be expressed as the sum of two terms, written as: $\phi = \phi_s + \phi_v$, where ϕ_s is the perturbation potential due to the rigid propeller rotating in the uniform flow, and ϕ_v is the perturbation potential due to the elastic propeller vibrating in the uniform flow. For detailed proof $\phi = \phi_s + \phi_v$, the reader may refer to Appendix A. The governing equations for the perturbation potential due to the rigid propeller rotating in the uniform flow can be written as:

$$\nabla^2 \phi_s = 0, \text{ in fluid domain } \Omega \quad (6)$$

$$\frac{\partial \phi_s}{\partial \mathbf{n}} = \mathbf{V}_0 \cdot \mathbf{n}, \text{ on blade surface } \Gamma \quad (7)$$

$$\Delta \phi_{s,w}(\mathbf{R}_{wake}) = \Delta \phi_s(\mathbf{R}_{re}), \text{ Morino Kutta condition} \quad (8)$$

The perturbation potential due to the rigid propeller rotating in the uniform flow can be calculated by using the given boundary equations. This gives the source and vorticity distributions on the surface of the blade. Then, the hydrodynamic forces generated by the uniform flow can be obtained by using Bernoulli's equation.

As the hydrodynamic forces generated by the uniform flow \mathbf{V}_0 is not important for the propeller vibration, in what follows, the formulation and implementation of the last part of the perturbation potentials ϕ_v are presented, leading to:

$$\mathbf{F}_w = \mathbf{F}_v \quad (9)$$

where \mathbf{F}_v represents the hydrodynamic force generated by the fluid-structure interaction, and the flow-induced added-mass and damping matrices can be derived from \mathbf{F}_v . In order to improve the computational efficiency, a frequency-dependent panel method is employed to determine the hydrodynamic pressure vector \mathbf{F}_v due to the structural deformation of the elastic blade.

2.3. Added-mass and -damping matrices

The governing equations for the perturbation potential due to the vibration of the flexible propeller in a uniform flow can be written as:

$$\nabla^2 \phi_v = 0 \text{ (in fluid domain } \Omega) \quad (10)$$

$$\frac{\partial \phi_v}{\partial \mathbf{n}} = -\frac{\partial \delta}{\partial t} \mathbf{n} + ((\delta \cdot \nabla) \mathbf{V}_0) \cdot \mathbf{n} \text{ (on blade surface } \Gamma) \quad (11)$$

$$\Delta \phi_{w,v}(\mathbf{R}_{wake}, t) = \Delta \phi_v(\mathbf{R}_{re}, t - t') \text{ (Morino Kutta condition)} \quad (12)$$

The perturbation velocity potential ϕ_v is governed by Laplace's equation. According to the Green's identity, ϕ_v can be calculated by the following integral expression:

$$\begin{aligned} 2\pi \phi_v(\mathbf{R}_P, t) &= \iint_{S_B} \phi_v(\mathbf{R}_Q, t) \frac{\partial G}{\partial \mathbf{n}_Q} d\mathbf{s} - \iint_{S_B} G \frac{\partial \phi_v(\mathbf{R}_Q, t)}{\partial \mathbf{n}_Q} d\mathbf{s} \\ &\quad + \iint_{S_w} \Delta \phi_{w,v}(\mathbf{R}_Q, t) \frac{\partial G}{\partial \mathbf{n}_Q} d\mathbf{s} \end{aligned} \quad (13)$$

where S_B and S_w denote the blade surface and wake sheet surface, respectively. In the present analysis, the thickness of the wake sheet surface is assumed as zero. The subscript Q corresponds to the variable point in the integration, and the subscript P represents the control point on the panel. \mathbf{R}_P and \mathbf{R}_Q are the position vectors of the points on the blade and wake sheet surface, respectively. $G(\mathbf{R}_P, \mathbf{R}_Q)$ is the Green's function,

which is the fundamental solution of Laplace equation in an unbounded 3-D fluid domain, given by: $G(\mathbf{R}_P, \mathbf{R}_Q) = 1/|\mathbf{R}_P - \mathbf{R}_Q| \cdot \mathbf{n}_Q$ is the outward unit normal vector. $\Delta \phi_{w,v}(\mathbf{R}_Q, t)$ represents the potential jump across the wake sheets.

Substituting Eq. (11) into Eq. (13), one obtains:

$$\begin{aligned} 2\pi \phi_v(\mathbf{R}_P, t) &- \iint_{S_B} \phi_v(\mathbf{R}_Q, t) \frac{\partial G}{\partial \mathbf{n}_Q} d\mathbf{s} - \iint_{S_w} \Delta \phi_{w,v}(\mathbf{R}_Q, t) \frac{\partial G}{\partial \mathbf{n}_Q} d\mathbf{s} \\ &= \iint_{S_B} G \left\{ -\frac{\partial \delta(\mathbf{R}_Q, t)}{\partial t} + [\delta(\mathbf{R}_Q, t) \cdot \nabla] \mathbf{V}_0 \right\} \cdot \mathbf{n}_Q d\mathbf{s} \end{aligned} \quad (14)$$

It is assumed that the frequency of excitation force F for the linear dynamic system is k , and $\delta(\mathbf{R}_Q, t) = \Re(\delta_k(\mathbf{R}_Q)e^{-ikt})$ is suitable, where \Re means the real part of the expression and $i = \sqrt{-1}$. Consequently, $\phi_v(\mathbf{R}_P, t)$ in above equation can be expressed as: $\phi_v(\mathbf{R}_P, t) = \Re(\phi_{k,v}(\mathbf{R}_P)e^{-ikt})$.

In this work, the radial interval of the blade from the hub to the tip is divided into N_r sub-intervals, and the chordwise interval from the leading edge to the trailing edge is decomposed into N_c sub-intervals. The strengths of the dipoles and sources are assumed to be uniform on the panel. The helical wake interval from the trailing edge to sufficient distance downstream is divided into N_w sub-intervals. The discretized form of Eq. (14) can be written as:

$$\mathbf{C}_{k,v}\{\phi_{k,v}\} = \mathbf{G}\{(ik\delta_k + (\delta_k \cdot \nabla) \mathbf{V}_0) \cdot \mathbf{n}\} \quad (15)$$

in which

$$\begin{aligned} \mathbf{C}_{k,v}(i, j) &= 2\pi \mathbf{I}(i, j) - \iint_{\Delta s_j} \frac{\partial G(\mathbf{R}_i, \mathbf{R}_j)}{\partial \mathbf{n}_j} d\mathbf{s} - \left(\sum_{j'=1}^{N_w} \iint_{\Delta s_j^j} e^{ikt_j^j} \frac{\partial G(\mathbf{R}_i, \mathbf{R}_j^j)}{\partial \mathbf{n}_j^j} d\mathbf{s} \right)_1 \\ &\quad + \left(\sum_{j'=1}^{N_w} \iint_{\Delta s_j^j} e^{ikt_j^j} \frac{\partial G(\mathbf{R}_i, \mathbf{R}_j^j)}{\partial \mathbf{n}_j^j} d\mathbf{s} \right)_2 \\ \{\phi_{k,v}\} &= [\phi_{k,v}(\mathbf{R}_1), \phi_{k,v}(\mathbf{R}_2), \dots, \phi_{k,v}(\mathbf{R}_N)]^T \\ \mathbf{G}(i, j) &= \iint_{\Delta s_j} \frac{1}{|\mathbf{R}_i - \mathbf{R}_j|} d\mathbf{s}, \quad i, j = 1, \dots, N; \quad N = 2N_r N_c \end{aligned}$$

and

$$\{(ik\delta_k + (\delta_k \cdot \nabla) \mathbf{V}_0) \cdot \mathbf{n}\} = \left[((ik\delta_k + (\delta_k \cdot \nabla) \mathbf{V}_0) \cdot \mathbf{n})|_{\mathbf{R}_1}, \right. \\ \left. ((ik\delta_k + (\delta_k \cdot \nabla) \mathbf{V}_0) \cdot \mathbf{n})|_{\mathbf{R}_2}, \dots, ((ik\delta_k + (\delta_k \cdot \nabla) \mathbf{V}_0) \cdot \mathbf{n})|_{\mathbf{R}_N} \right]^T$$

where \mathbf{I} is a $N \times N$ identity matrix. Δs_j is the area of the j th panel. Δs_j^j is the area of the j th panel on the j th vortex strip. \mathbf{n}_j is the outward unit normal vector of the j th panel on the blade, and \mathbf{n}_j^j is the unit normal vector of the j th panel on j th vortex strip. \mathbf{R}_i represents the position vector of the control point on the i th panel, and \mathbf{R}_j^j denotes the position vector of the control point on the j th panel of the j th vortex strip. t_j^j represents the time required for the vortex moving from the panel on trailing edge to the j th panel on j th vortex strip. The subscript 1 indicates that the formula is only calculated for the panels on the trailing edge of the suction surface, whereas the subscript 2 indicates that the formula is employed for panels on the trailing edge of the pressure surface. N is the total number of panels.

Since small blade vibration is considered, the distance change in the Green's function is negligible. Hence, one obtains:

$$\begin{aligned} \{\phi_{k,v}\} &= \mathbf{C}_{k,v}^{-1} \mathbf{G}\{(ik\delta_k + (\delta_k \cdot \nabla) \mathbf{V}_0) \cdot \mathbf{n}\} \\ &= \mathbf{U}(ik\{\delta_{kn}\} + \mathbf{D}\{\delta_k\}) \end{aligned} \quad (16)$$

where

$$\mathbf{U} = \mathbf{C}_{k,v}^{-1} \mathbf{G}$$

$$\delta_{kn} = \delta_k \cdot \mathbf{n}$$

$$\mathbf{D} = \left[\begin{array}{ccc} \left(\frac{\partial \mathbf{V}_0}{\partial x} \cdot \mathbf{n} \right) \Big|_1 & \left(\frac{\partial \mathbf{V}_0}{\partial y} \cdot \mathbf{n} \right) \Big|_1 & \left(\frac{\partial \mathbf{V}_0}{\partial z} \cdot \mathbf{n} \right) \Big|_1 \\ & \ddots & \\ & & \left(\frac{\partial \mathbf{V}_0}{\partial x} \cdot \mathbf{n} \right) \Big|_N & \left(\frac{\partial \mathbf{V}_0}{\partial y} \cdot \mathbf{n} \right) \Big|_N & \left(\frac{\partial \mathbf{V}_0}{\partial z} \cdot \mathbf{n} \right) \Big|_N \end{array} \right]$$

$$\{\delta_k\} = [\delta_k(\mathbf{R}_1), \delta_k(\mathbf{R}_2), \dots, \delta_k(\mathbf{R}_N)]^T$$

$$\{\delta_{kn}\} = [\delta_k(\mathbf{R}_1) \cdot \mathbf{n}(\mathbf{R}_1), \delta_k(\mathbf{R}_2) \cdot \mathbf{n}(\mathbf{R}_2), \dots, \delta_k(\mathbf{R}_N) \cdot \mathbf{n}(\mathbf{R}_N)]^T$$

By applying the momentum equation of the fluid, Bernoulli's equation can be based on the potential flow theory, given as:

$$p = p_0 + \rho \left(\frac{1}{2} \mathbf{V}_0^2 - \frac{1}{2} \mathbf{V}_{total}^2 - \frac{\partial \phi_v}{\partial t} \right) \quad (17)$$

where p_0 is the absolute hydrostatic pressure at the computational point, and ρ is the fluid density. In the present model, the absolute hydrostatic pressure is not important. In addition, when the vibration-induced perturbation velocity $\nabla \phi_v$ is small, higher-order terms in Eq. (17) can be neglected. In such a case, Eq. (17) can be rewritten as:

$$p = -\rho \left(\frac{\partial \phi_v}{\partial t} + \mathbf{V}_0 \cdot \nabla \phi_v \right) \quad (18)$$

Note Eq. (18) is the linear Bernoulli formula. It is applied to determine the pressure due to small deformations. There are two ways to calculate the unsteady pressure based on the linear Bernoulli formula. One is using differential operation on the blade surface to calculate $\nabla \phi_v$, and the other is using a direct integration method which requires robust numerical treatment of six singular integrals; for more details, the reader is referred to Gao (2005), Hassan Ghassemi and Kohansal (2009), Hess and Smith (1967, 1964) and Tarafder et al. (2010). The direct integration method is employed herein. In doing so, $\nabla \phi_v$ can be calculated by taking the l th component of the spatial derivative of Eq. (14) as follows:

$$\begin{aligned} 2\pi \frac{\partial \phi_v(\mathbf{R}_P, t)}{\partial x_l} - \int_{S_B} \phi_v(\mathbf{R}_Q, t) \frac{\partial}{\partial x_l} \left(\frac{\partial G(\mathbf{R}_P, \mathbf{R}_Q)}{\partial \mathbf{n}_Q} \right) ds \\ - \int_{S_w} \Delta \phi_{w,v}(\mathbf{R}_Q, t) \frac{\partial}{\partial x_l} \left(\frac{\partial G(\mathbf{R}_P, \mathbf{R}_Q)}{\partial \mathbf{n}_Q} \right) ds \\ = \int_{S_B} \left(-\frac{\partial \delta(\mathbf{R}_Q, t)}{\partial t} \cdot \mathbf{n}_Q + ((\delta(\mathbf{R}_Q, t) \cdot \nabla) \mathbf{V}_0) \cdot \mathbf{n}_Q \right) \frac{\partial}{\partial x_l} (G(\mathbf{R}_P, \mathbf{R}_Q)) ds \end{aligned} \quad (19)$$

Substituting Eq. (12) and Eq. (16) into Eq. (19), the discretized form of Eq. (19) can be written as:

$$\begin{aligned} \left\{ \frac{\partial \phi_{k,v}}{\partial x_l} \right\} &= \mathbf{C}_{k,v}^{x_l} \mathbf{U} (ik\{\delta_{kn}\} + \mathbf{D}\{\delta_k\}) + \mathbf{G}^{x_l} (ik\{\delta_{kn}\} + \mathbf{D}\{\delta_k\}) \\ &= \mathbf{U}^{x_l} (ik\{\delta_{kn}\} + \mathbf{D}\{\delta_k\}), \mathbf{U}^{x_l} = \mathbf{C}_{k,v}^{x_l} \mathbf{U} + \mathbf{G}^{x_l} \end{aligned} \quad (20)$$

where \mathbf{U}^x is the combined influence coefficient matrix and the other formulas are given as follows:

$$\begin{aligned} \left\{ \frac{\partial \phi_{k,v}}{\partial x_l} \right\} &= \left[\frac{\partial \phi_{k,v}}{\partial x_l} (\mathbf{R}_1), \dots, \frac{\partial \phi_{k,v}}{\partial x_l} (\mathbf{R}_N) \right]^T \\ \mathbf{G}^{x_l}(i,j) &= \frac{1}{2\pi} \iint_{\Delta s_j} \frac{\partial G(\mathbf{R}_i, \mathbf{R}_j)}{\partial x_l} ds; i, j = 1, \dots, N \\ \mathbf{C}_{k,v}^{x_l}(i,j) &= \frac{1}{2\pi} \left(\begin{aligned} &\iint_{\Delta s_j} \frac{\partial}{\partial x_l} \left(\frac{\partial G(\mathbf{R}_i, \mathbf{R}_j)}{\partial \mathbf{n}_j} \right) ds \\ &+ \left(\sum_{j'=1}^{N_w} \iint_{\Delta s_{j'}} e^{ikr_j'} \frac{\partial}{\partial x_l} \left(\frac{\partial G(\mathbf{R}_i, \mathbf{R}_{j'})}{\partial \mathbf{n}_{j'}} \right) ds \right)_1 \\ &- \left(\sum_{j'=1}^{N_w} \iint_{\Delta s_{j'}} e^{ikr_j'} \frac{\partial}{\partial x_l} \left(\frac{\partial G(\mathbf{R}_i, \mathbf{R}_{j'})}{\partial \mathbf{n}_{j'}} \right) ds \right)_2 \end{aligned} \right) \end{aligned}$$

Substituting Eq. (16) and Eq. (20) into the linearized Bernoulli Eq. (18), one obtains the dynamic pressure as:

$$\{p_v(k)\} = \Re \left(-\rho e^{-ikt} \left(\begin{aligned} &ik \left(-\mathbf{UD}\{\delta_k\} + \sum_{l=1}^3 \mathbf{V}_0^{x_l} \mathbf{U}^{x_l} \{\delta_{kn}\} \right) \\ &+ k^2 \mathbf{U}\{\delta_{kn}\} + \sum_{l=1}^3 \mathbf{V}_0^{x_l} \mathbf{U}^{x_l} \mathbf{D}\{\delta_k\} \end{aligned} \right) \right) \quad (21)$$

where $\mathbf{V}_0^{x_l} = \text{diag}\{V_{0x_l}(\mathbf{R}_1), \dots, V_{0x_l}(\mathbf{R}_N)\}$, and $V_{0x_l}(\mathbf{R}_i)$ is the component of \mathbf{V}_0 in the x_l direction on point \mathbf{R}_i . The pressure vector in Eq. (21) is expressed in terms of the unknown displacement vectors $\{\delta_k\}$ and $\{\delta_{kn}\}$, which are calculated at blade panel centroids.

It is necessary to express the pressure vector in terms of the blade nodal displacements in the finite element model, and to apply the pressure of the fluid on the finite element nodes of the blade. For convenience, the mesh of finite element model is coincident with that of panel model on the blade surface. Assuming $\{\delta_k\} = \mathbf{Z}_2 \mathbf{u}_k$ and $\{\delta_{kn}\} = \mathbf{Z}_1 \mathbf{u}_k$, where \mathbf{Z}_1 and \mathbf{Z}_2 are shape function matrices, and \mathbf{u}_k is the nodal displacement vector, the dynamic force can be calculated as:

$$\mathbf{F}_v(k) = \Re \left(\rho \mathbf{Z}_1^T \Delta s e^{-ikt} \left(\begin{aligned} &ik \left(-\mathbf{UDZ}_2 \mathbf{u}_k + \sum_{l=1}^3 \mathbf{V}_0^{x_l} \mathbf{U}^{x_l} \mathbf{Z}_1 \mathbf{u}_k \right) \\ &+ k^2 \mathbf{UZ}_1 \mathbf{u}_k + \sum_{l=1}^3 \mathbf{V}_0^{x_l} \mathbf{U}^{x_l} \mathbf{DZ}_2 \mathbf{u}_k \end{aligned} \right) \right) \quad (22)$$

where Δs is a diagonal matrix given by: $\Delta s = \text{diag}\{\Delta s_1, \Delta s_2, \dots, \Delta s_N\}$. Δs_i is the i th panel area.

In order to calculate the vibratory perturbation potential $\phi_{k,v}$ and the hydroelastic force $\mathbf{F}_v(k)$ via the panel method, the three-dimensional nodal displacement vector \mathbf{u}_k is needed from the finite element model. In turn, the finite element analysis for the structural responses (displacement \mathbf{u}_k , velocity $\dot{\mathbf{u}}_k$ and acceleration $\ddot{\mathbf{u}}_k$) of the propeller requires the hydrodynamic force $\mathbf{F}_v(k)$ from the analysis of the panel method. In this study, the fluid-structure interaction problem is solved by placing the hydroelastic force to the left-hand side of the equilibrium equation of motion, given as:

$$[\mathbf{M} + \mathbf{M}_W(k)]\ddot{\mathbf{u}}_k + [\mathbf{C} + \mathbf{C}_W(k)]\dot{\mathbf{u}}_k + \mathbf{K}\mathbf{u}_k = \mathbf{F} \quad (23)$$

where $\mathbf{M}_W(k)$ and $\mathbf{C}_W(k)$ are the added-mass and added-damping matrix respectively, given as

$$\mathbf{M}_W(k) = \frac{\rho}{k^2} \mathbf{Z}_1^T \Delta s \left\{ \begin{array}{l} k^2 \Re(\mathbf{U}) \mathbf{Z}_1 + \sum_{l=1}^3 \mathbf{V}_0^{x_l} \Re(\mathbf{U}^{x_l}) \mathbf{DZ}_2 \\ -k \left[-\Im(\mathbf{U}) \mathbf{DZ}_2 + \sum_{l=1}^3 \mathbf{V}_0^{x_l} \Im(\mathbf{U}^{x_l}) \mathbf{Z}_1 \right] \end{array} \right\} \quad (24)$$

$$\mathbf{C}_W(k) = \frac{\rho}{k} \mathbf{Z}_1^T \Delta s \left\{ \begin{array}{l} k^2 \Im(\mathbf{U}) \mathbf{Z}_1 + \sum_{l=1}^3 \mathbf{V}_0^{x_l} \Im(\mathbf{U}^{x_l}) \mathbf{DZ}_2 + \\ k \left[-\Re(\mathbf{U}) \mathbf{DZ}_2 + \sum_{l=1}^3 \mathbf{V}_0^{x_l} \Re(\mathbf{U}^{x_l}) \mathbf{Z}_1 \right] \end{array} \right\} \quad (25)$$

where \Im represents the imaginary part of an expression.

2.5. Numerical algorithm for the governing equations

For solving Eq. (23), the direct time-integration methods, such as Wilson-θ and Newmark-β method can be employed. However, the matrix dimension of Eq. (23) is generally high, and the computation resources required by these methods for solving Eq. (23) are time-consuming. It is to note that the modal superposition method is an efficient method for structural dynamics analysis. Unfortunately, the added-mass and -damping matrices in Eq. (23) are asymmetric matrices and therefore, Eq. (23) may not be calculated by modal superposition method directly. A HRZ-like lumping technique (Young, 2007) may be used, which replaces $\mathbf{M}_W(k)$ and $\mathbf{C}_W(k)$ with the diagonal added matrices $\mathbf{M}_W^D(k)$ and $\mathbf{C}_W^D(k)$. However, this method may be inaccurate to predict the vibration modes of the propeller blades (will be discussed in the subsequent sections).

We assume that the first N_{mode} wet mode vectors of the elastic propeller can be collected into a modal matrix, given as: Ψ_k , and the modal vectors ψ_k^i satisfies the following equation:

$$(-\omega_i^2(k)(\mathbf{M} + \mathbf{M}_W(k)) + \mathbf{K})\psi_k^i = 0, i = 1, 2, \dots, N_{mode} \quad (26)$$

Assuming $\mathbf{u}_k = \sum_{i=1}^{N_{mode}} q_k^i(t)\psi_k^i$, Eq. (23) can be rewritten as:

$$\widehat{\mathbf{M}}_k \ddot{\mathbf{q}}_k(t) + \widehat{\mathbf{C}}_k \dot{\mathbf{q}}_k(t) + \widehat{\mathbf{K}}_k \mathbf{q}_k(t) = \widehat{\mathbf{F}} \quad (27)$$

where

$$\begin{aligned} \Psi_k &= \{\psi_k^1, \psi_k^2, \dots, \psi_k^{N_{mode}}\} \\ \mathbf{q}_k(t) &= [q_k^1(t), q_k^2(t), \dots, q_k^{N_{mode}}(t)]^T \\ \widehat{\mathbf{M}}_k &= \Psi_k^T [\mathbf{M} + \mathbf{M}_W(k)] \Psi_k \\ \widehat{\mathbf{C}}_k &= \Psi_k^T [\mathbf{C} + \mathbf{C}_W(k)] \Psi_k \\ \widehat{\mathbf{K}}_k &= \Psi_k^T \mathbf{K} \Psi_k \\ \widehat{\mathbf{F}} &= \Psi_k^T \mathbf{F} \end{aligned}$$

The degrees of freedom of the system have been reduced to N_{mode} . By applying Wilson-θ method, $\mathbf{q}_k(t)$ in Eq. (27) can be solved very efficiently. Once $\mathbf{q}_k(t)$ is determined, then \mathbf{u}_k can be calculated by using the following formula:

$$\mathbf{u}_k = \sum_{i=1}^{N_{mode}} q_k^i(t) \psi_k^i$$

3. Validation

3.1. FEM validation

3.1.1. Free vibration analysis

To confirm the validity of the structural modeling, the numerical results obtained from the present method for one blade of the propeller 4119 are compared with those solutions obtained using ANSYS (Fig. 2). The blade is fixed at the root and the geometrical configuration is shown in Fig. 2. For free vibration analysis, the structural damping of the blade is neglected. The structural mesh of the blade surface is the same as that used in panel modeling for the fluid, and a uniform mesh is employed in the thickness direction of the blade. In order to discretize the propeller by using the three-dimensional linear isoparametric elements of eight nodes, two edges of the propeller are cut in the present model, which are vertical to the chord of the propeller and are located at 0.0002 of the chord length measured from the leading edge and 0.9998 measured from the trailing edge. A considerable number of numerical tests have been performed, and the results show that the effect of above mentioned cutting on the dynamic behaviors of the propeller can be neglected. The results shown in Figs. 3 and 4 are obtained by discretizing the blade into 2, 40 and 40 elements in the thickness, radial and chordwise directions, respectively. In the commercial software ANSYS, the SOLID 185 elements are employed for the discretization of the propeller, and the finite element model consists of a total of 54592 tetrahedral elements. The computed natural frequencies and mode shapes are presented in Figs. 3 and 4. The results show that the present solutions agree well with those obtained from ANSYS.

In order to further validate the accuracy of the present method for

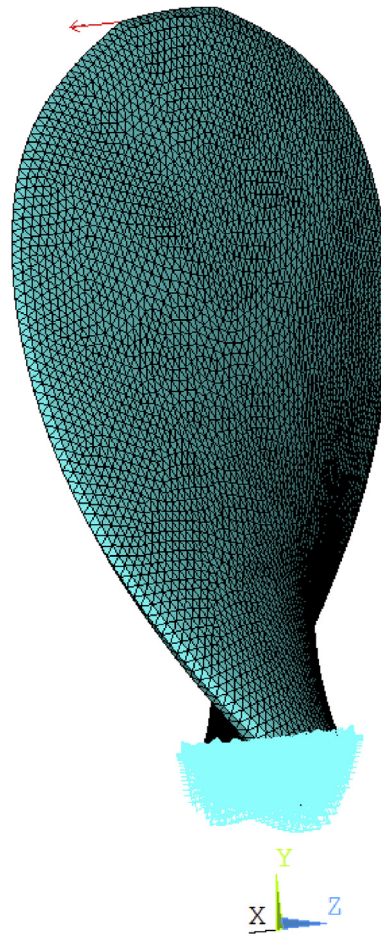


Fig. 2. Discretization of one blade of propeller 4119 and its calculation model in ANSYS.

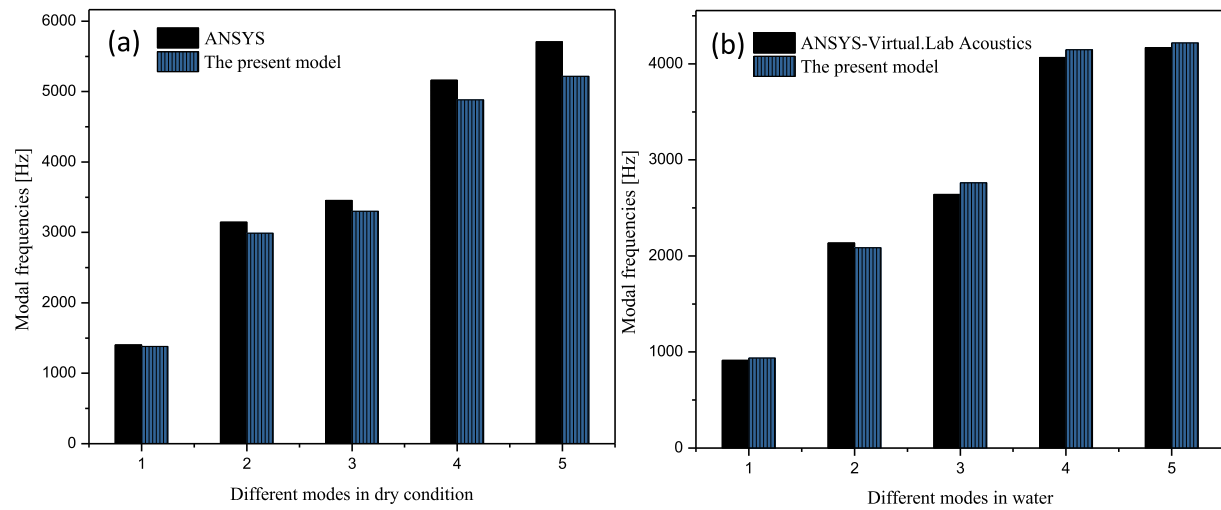


Fig. 3. Comparison of natural frequencies predicted by the present method and those of ANSYS/Virtual.Lab Acoustics. (a) dry modes; (b) wet modes.

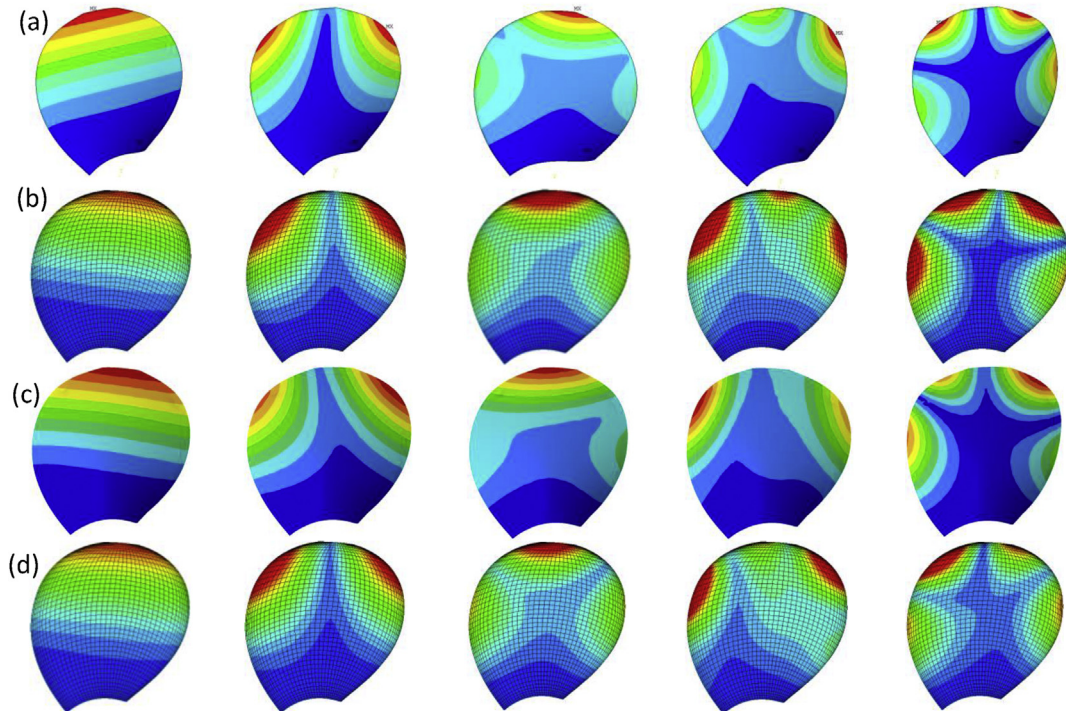


Fig. 4. Comparison of mode shapes of the propeller: (a) dry mode shapes by ANSYS; (b) dry mode shapes by present method; (c) wet mode shapes by ANSYS-Virtual.Lab Acoustics; (d) wet mode shapes by present method.

calculating the natural frequencies of the propellers, the fundamental frequencies of two 7-blade high skew model propellers in both dry and wet conditions were examined here. These two propellers are made of bronze and plastic materials, which follow the same geometrical configurations as shown in Fig. 5. The diameter of the two propellers is taken as 250 mm. Regarding the details of the geometrical and material parameters of the propellers, the reader may refer to Tian et al. (2017, 2016). The computed fundamental frequencies for the two propellers are given in Table 1, and the experimental data reported by Tian et al. (2017, 2016) are also provided in the table for comparison purpose. It is observed from Table 1 that the present results are in very good agreement with the experimental data, and the maximum discrepancy is less than 2.56% for all the cases considered. This confirms the validity of the present method.

3.1.2. Forced vibration analysis

The force applied at the end of one blade of propeller 4119 is illustrated in Fig. 2, which is defined as: $f = \sin(2\pi f_0 t)N$, and f_0 is the driving frequency of the force, taken as $f_0 = 1000$ Hz. The displacement responses of the blade measured in three directions (namely, x , y and z directions) at the same point are presented in Fig. 6(a). The reaction forces measured at the root of the blade in x , y and z directions are presented in Fig. 7. The present results are obtained by discretizing the blade into 2, 40 and 40 elements in the thickness, radial and chordwise directions, respectively. It is observed from Figs. 6(a) and 7 that the present results are in good agreement with those obtained from ANSYS.

3.2. Fluid–structure interaction analysis

This section is devoted to the validation of the fluid-structure

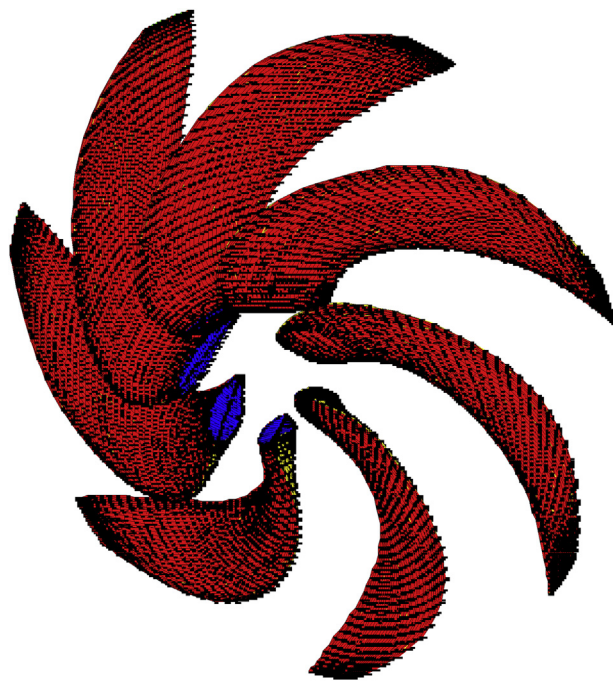


Fig. 5. Boundary element mesh of the 7-blade high skew model propeller.

Table 1

Fundamental frequencies (Hz) of the two 7-blade high skew model propellers obtained by experimental method and present numerical model.

	Dry condition		Wet condition	
	Experiment	Present method	Experiment	Present method
Plastic propeller	195.2	190.2	79.7	77.9
Bronze propeller	519.1	516.8	388.4	392.8

interaction analysis. The added-mass and added-damping matrices are examined. Although it's difficult to check these two fluid-structure coupling matrices directly, they may be validated implicitly by examining the natural frequencies, mode shapes and dynamic responses of the propeller in a stationary flow.

The natural frequencies, mode shapes and dynamic responses are obtained for the same blade of propeller 4119 as considered in Sec. 3.1

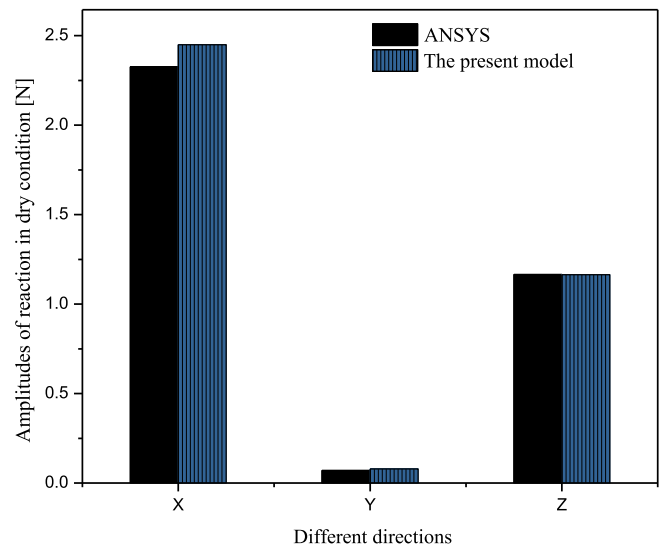


Fig. 7. Reaction force amplitudes of blade in dry condition predicted by the present model and ANSYS.

(see Fig. 2), except that the blade is immersed in a stationary water now. It can be inferred from Appendix B that the vibration modes of the blade based on the fluid-structure interaction analysis in stationary flow are the same as those based on the acoustic-solid interaction analysis when the speed of sound of the fluid is set to infinity, and the displacement responses calculated by the two methods for the same material point in the blade will be equal to each other. The present results determined by the fluid-structure interaction analysis are compared with the numerical solutions obtained from the acoustic-solid interaction analysis by using ANSYS and Virtulab.Lab Acoustics. In the commercial software packages, the finite element model of the propeller follows the same configuration as considered in the previous section. The water surrounding the propeller is modeled with 1371 linear boundary elements, including 1201 four-node planar elements and 70 three-node triangular elements. A mortar method (Peters et al., 2012) is employed to enforce the coupling of the non-conforming structural and acoustic meshes. For details on the derivation of the FE/BE equations for the fully coupled structural-acoustic system, the reader is referred to Peters et al. (2012). Comparisons of the natural frequencies, mode shapes and displacement amplitudes obtained by different methods are shown in Fig. 3(b), Figs. 4(c)–(d) and Fig. 6(b). The results show that the present solutions are in very agreement with those obtained from ANSYS and Virtulab.Lab

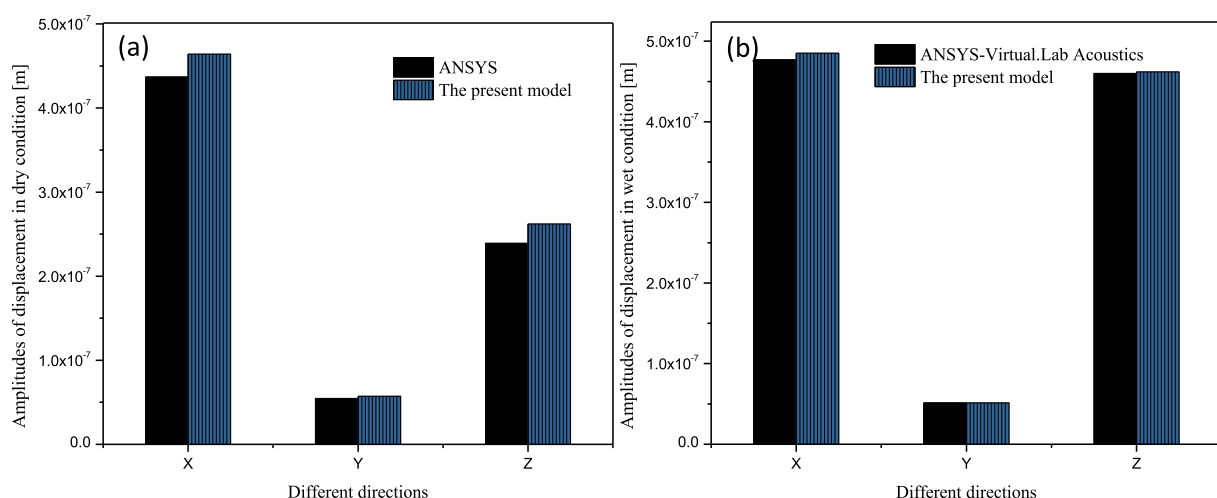


Fig. 6. Displacement amplitudes of blade predicted by the present model and ANSYS/Virtual.Lab Acoustics. (a) dry condition; (b) wet condition.

Table 2

Comparison of the first five wet modes of the propeller calculated by ANSYS-Virtual. Lab Acoustics, present method and HRZ-like model (Hz).

Mode number	ANSYS-Virtual.Lab Acoustics	Present method	HRZ-like model
1	914.3	935.9	996.2
2	2135.3	2085.3	1663.3
3	2641.9	2760.2	2 171.4
4	4 066.9	4146.7	2 672.1
5	4168.3	4217.4	2 803.6

Acoustics. In addition, it can be observed from Table 1 that the computed fundamental frequencies of these two 7-blade high skew model propellers in wet condition agree well with those experimental data. This further validate the accuracy of the present method. For additional comparison, the natural frequencies determined by using the HRZ-like symmetrization method are displayed in Table 2 and the results are compared with the numerical solutions. It is observed from Table 2 that the HRZ-like method is not accurate for predicting the vibration modes of the blade.

In order to further validate the added mass and damping coefficient matrices obtained by the present method, the axial oscillation problems of rigid propellers are examined. It is to note that the elements of added matrices, $[\mathbf{M}_W(k)]_{ij}$ and $[\mathbf{C}_W(k)]_{ij}$, represent the hydrodynamic forces acting on the blade nodes due to the nodal accelerations and velocities. With the numbering of the vector components for the blade surface points being in x, y and z sequence, the first row of the matrix $\mathbf{M}_W(k)$, for example, represents the water inertia forces in x direction at nodal point 1. This implies that if one specify a unit axial harmonic oscillation of the propeller and a summation over the axial forces generated by all nodal points, the total axial added mass of a rigid propeller can be obtained. Added damping of rigid propeller can be determined by the same way. For a rigid propeller, the added mass and damping by axial oscillation can be obtained by:

$$\mathbf{M}_A = \mathbf{\Lambda} \mathbf{M}_W(k) \mathbf{\Lambda}^T \quad (28)$$

$$\mathbf{C}_A = \mathbf{\Lambda} \mathbf{C}_W(k) \mathbf{\Lambda}^T \quad (29)$$

where \mathbf{M}_A and \mathbf{C}_A are the added mass and damping due to the axial oscillation of the propeller, respectively. $\mathbf{\Lambda}$ is defined as: $\mathbf{\Lambda} = [1 \ 0 \ 0 \ 1 \ 0 \ 0 \ \dots \ 1 \ 0 \ 0]$.

The added mass and damping of the propeller 4381 under rigid axial oscillation are calculated. The following parameters are employed in the computation: advance ratio $J = 0.889$, rotating speed $n = 11.519$ rad/s and excitation frequency $f = 9.17$ Hz. The present results are compared with those obtained by Mao and Young (2016); Parsons et al. (1980) and Schwanecke (1963). It is to note that Mao and Young (2016) used a 3-D curved lifting line method, while Parsons et al. (1980) and Schwanecke (1963) employed semi-empirical models. The computed results for the added mass and damping are shown in Table 3. The computed results are compared well with those reference solutions, which further confirms the validity of our method.

The convergence of the unsteady axial reactions against the grid size for the propeller 4381 in wet condition is shown in Table 4, where N_w , N_d , N_r and N_c represent the number of elements discretized in the wake, thickness, radial, chordwise directions of the propeller, respectively. N_{mode} is the mode number used in the modal reduction technique and $|F_x|$

Table 4

Comparison of unsteady axial reactions of propeller in wet condition using different grid sizes.

Mesh ($N_{mode} \times N_w \times N_t \times N_r \times N_c$)	$ F_x (N)$
$200 \times 800 \times 3 \times 20 \times 20$	2.72
$1\ 000 \times 800 \times 3 \times 20 \times 20$	2.59
$400 \times 800 \times 3 \times 20 \times 20$	2.59
$400 \times 1\ 200 \times 3 \times 20 \times 20$	2.53
$400 \times 400 \times 3 \times 20 \times 20$	2.71
$400 \times 800 \times 4 \times 20 \times 20$	2.53
$400 \times 800 \times 2 \times 20 \times 20$	2.77
$400 \times 800 \times 3 \times 36 \times 34$	1.88
$400 \times 800 \times 3 \times 26 \times 20$	1.88

represents the amplitude of the unsteady axial reaction. The advance ratio and the inflow velocity employed for the computation are taken as $J = 0.8$ and $V = 10$ m/s, respectively. The material data of the propeller are given as: Young's modulus $E = 210$ GPa, Poisson's ratio $\nu = 0.3$, and density $\rho_s = 7800\text{kg/m}^3$. The density of the fluid is assumed as: $\rho = 1000\text{kg/m}^3$. The driving frequency of the force is taken as 1300 Hz, and its magnitude is 1 N. The driving force is applied at the tip of the leading edge of the blade, which is acting in positive x -direction, as shown in Fig. 1. It can be found that the numerical solutions converge very rapidly as the number of finite elements and the number of the vibration modes truncated in the superposition method are increased. The results show that the mesh $400 \times 800 \times 3 \times 26 \times 20$ can be used to obtain reasonably accurate results, and this mesh will be employed in the following analysis.

4. Results and discussions

4.1. The added mass characteristics

4.1.1. Influence of excitation frequency

The frequency-domain panel method in conjunction with the FEM method has been employed to investigate the effect of excitation frequency on the wet modes (added mass) of the propeller. Only one blade of propeller 4381 is considered here. The blade has a diameter D of 0.25 m and advance ratio $J(J = V/nD)$ of 0.8, where n denotes the rotational speed of the propeller. The inflow velocity V is assumed as: 10 m/s. The material parameters of the propeller are given as follows: Young's modulus $E = 210$ GPa, density $\rho_s = 7800\text{kg/m}^3$, and Poisson's ratio $\nu = 0.3$. The density of the fluid is: $\rho = 1000\text{kg/m}^3$. The structural damping of the propeller is neglected. The driving frequencies of the force are specified as: $f_0 = 8, 50, 1300$ Hz. For the propeller either in dry condition or wet condition, the first ten natural frequencies of the propeller predicted by the present method are shown in Fig. 8. To demonstrate the effect of the boundary condition term $((\delta \cdot \nabla) \mathbf{V}_0) \cdot \mathbf{n}$, the imaginary parts of the added mass and the movement of the fluid on the vibrations of the blade, five numerical models are examined here, which are labeled as Model #1, #2, #3, #4 and #5. The added terms generated by $((\delta \cdot \mathbf{V}_0) \cdot \mathbf{n}) (\mathbf{D} \neq 0)$ and the imaginary part of the added mass are included in Model #1. In Model #2, the added terms generated by $((\delta \cdot \mathbf{V}_0) \cdot \mathbf{n}) \mathbf{is}$ considered ($\mathbf{D} \neq 0$) but imaginary part of added mass is neglected. For Model #3, the added terms generated by $((\delta \cdot \mathbf{V}_0) \cdot \mathbf{n}) \mathbf{is}$ neglected ($\mathbf{D} = 0$) and imaginary part of added mass is considered. In the case of Model #4, both the added terms due to $((\delta \cdot \mathbf{V}_0) \cdot \mathbf{n})$ and imaginary part of added mass are neglected ($\mathbf{D} = 0$). Static water is considered for Model #5. Note that the natural frequencies of the propeller in dry condition are the inherent feature of the structure. However, the main focus considered here is to compare the wet and dry modes of the propeller. These modes do not vary against with the advance ration, inflow velocity and excitation frequency. In this work, only the effect of the excitation frequency under the condition of a fixed high inflow velocity and advance ratio is examined.

From Fig. 8, the following conclusions can be drawn:

Table 3

Comparison of the added coefficients generated by axial oscillation of the propeller.

Coefficients	Present method	Mao and Young (2016)	Parsons et al. (1980)	Schwanecke (1963)
M_A	0.0709	0.08252	0.07639	0.09205
C_A	0.5462	0.60815	0.67274	1.32021

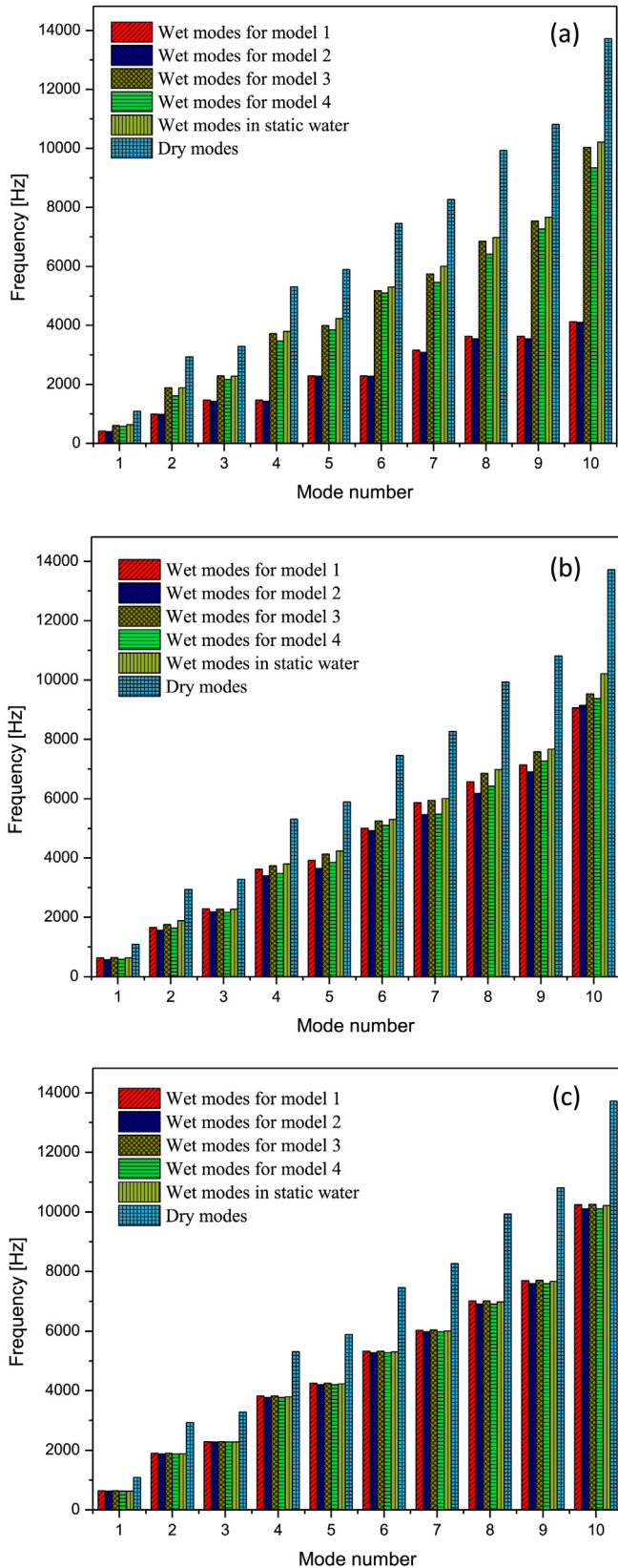


Fig. 8. Comparison of the first ten modes of propeller 4381 blade predicted by different models ($J = 0.8$ and $V = 10$ m/s). (a) $f = 8$ Hz; (b) $f = 50$ Hz; (c) $f = 1300$ Hz.

- (1) Imaginary part of the added-mass matrix can be neglected. In addition, $((\delta \cdot \nabla) \mathbf{V}_0) \cdot \mathbf{n}$ is important at lower excitation frequencies, which indicates that the non-penetration conditions should be

satisfied on the deformed blade surface rather than on the undeformed one at lower excitation frequencies.

- (2) Due to the existence of the fluid-structure interaction, the natural frequencies related to the wet modes are significantly smaller than those of the dry modes. This indicates that the wet modes must be employed for predicting the unsteady performance of an elastic propeller, even though the deformation of the propeller is small. The decrease in the fundamental frequency of the propeller may lead to resonance of the propeller at lower frequencies, resulting in high amplitude of the hydrodynamic forces.
- (3) The term of $\rho Z_1^T \Delta s \Re(\mathbf{U}) Z_1$ is sufficient to determine the main feature of the added mass at high excitation frequency. Moreover, the difference between static and flowing water lies in the wake term of \mathbf{U} , which is not significant if the inflow velocity is not large.

4.1.2. Influence of flow velocity and material property

In order to investigate the effect of the flow velocity on the wet modes (added mass) of the blade, the same blade considered in Sec. 4.1.1 is examined in the following study. The excitation frequencies considered here are 2 Hz (low frequency) and 1300 Hz (high frequency). In the previous case, six models used in Sec. 4.1.1 are displayed, and the inflow velocity V is specified as 0.02, 0.2, 1 m/s as shown in Fig. 9. However, only for Model #1, the wet condition in static water, and dry condition are applied in the high frequency situation as shown in Fig. 10 and the inflow velocity V is specified as 0.02, 2, 6, 10, 20 and 50 m/s. In Fig. 10, the effect of the elastic modulus E on the added mass is also examined. By applying advance ratio $J = V/nD = 0.8$, the rotating speed of the propeller in all above cases can be determined.

It is observed from Fig. 9 that the term $((\delta \cdot \nabla) \mathbf{V}_0) \cdot \mathbf{n}$ is important at lower excitation frequencies when the inflow velocity is relative large. When the inflow velocity is small enough, the added mass may be determined by $\rho Z_1^T \Delta s \Re(\mathbf{U}) Z_1$ or by considering the wet condition in static water. The results in Fig. 10 show that for the propeller in dry condition or in wet condition, the vibration modes will decrease as the elastic modulus reduced. The term of $\rho Z_1^T \Delta s \Re(\mathbf{U}) Z_1$ or the static water case is a good approximation for predicting the wet modes of propeller. However, when the inflow velocity is relative large, the wet modes of the propeller obtained from $\rho Z_1^T \Delta s \Re(\mathbf{U}) Z_1$ will be lower than those obtained from the wet condition in static water. It is observed from Fig. 10 and Table 5 that the velocity has little effect on the lower vibration modes of the propeller. For example, the first vibration mode of the propeller for the case of $V = 50$ m/s decreases only by 0.022% compared to the wet modes of the propeller in stationary water. However, this is not the case for higher vibration modes of the propeller. For example, the tenth mode of the propeller under $V = 50$ m/s decreases by 2.71% compared to the wet modes of the propeller in stationary water. In addition, the results in Table 5 show that the elastic modulus of the propeller has little effect on the ratios $(f_{air} - f_{water}|_{V=0})/f_{air}$ and $(f_{water}|_{V=0} - f_{water}|_{V=50})/f_{water}|_{V=0}$. The ratio $(f_{air} - f_{water}|_{V=0})/f_{air}$ describes the decrease of the wet mode frequencies of the propeller in stationary water compared to those corresponding to the dry modes, and $(f_{water}|_{V=0} - f_{water}|_{V=50})/f_{water}|_{V=0}$ denotes the decrease of the wet mode frequencies of the propeller for $V = 50$ m/s compared to those of the propeller in stationary water. This can be explained by the linear theory of elasticity under the framework of small deformation considered here.

4.1.3. Influence of advance ratio

The effect of advance ratio on the added mass is investigated here, and the computed results are illustrated in Fig. 11. The same blade considered in Sec. 4.1.2 is examined. The excitation frequency of the driving force is taken as 1300 Hz, and elastic modulus of the propeller is assumed as: $E = 210$ GPa. In order to investigate the effect of the advance ratio on the added mass of the propeller, the inflow velocity V is specified as 10 and 50 m/s, and three different advance ratios are considered, given

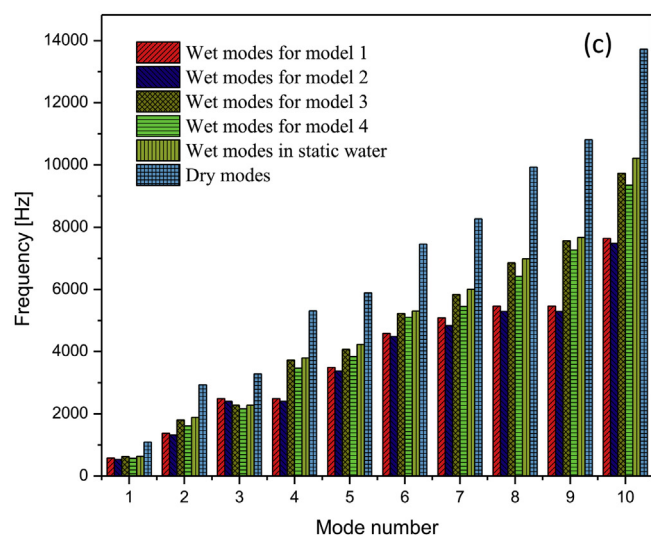
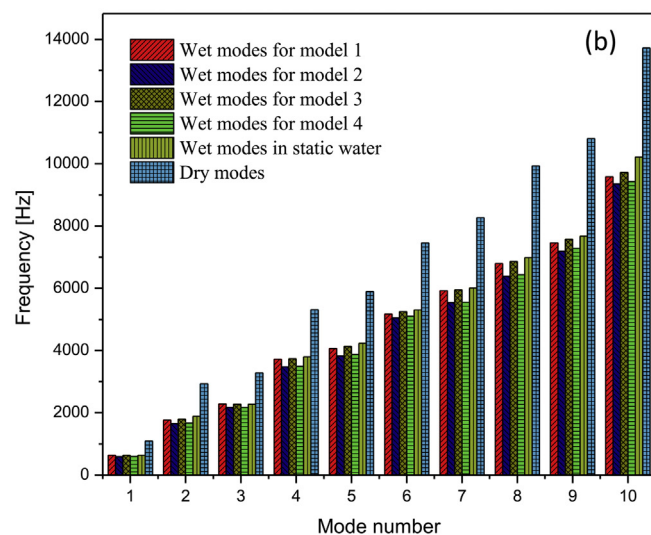
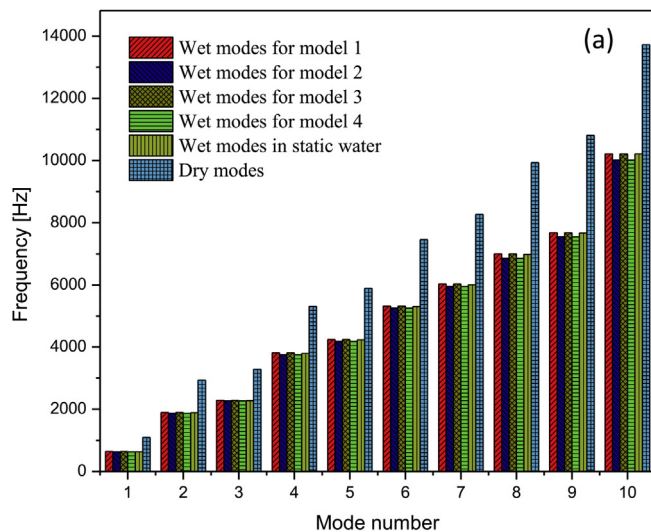


Fig. 9. Comparison of the first ten modes of propeller 4381 blade ($J = 0.8$, $E = 210$ GPa and $f = 2$ Hz): (a) $V = 0.02$ m/s; (b) $V = 0.2$ m/s; (c) $V = 1$ m/s.

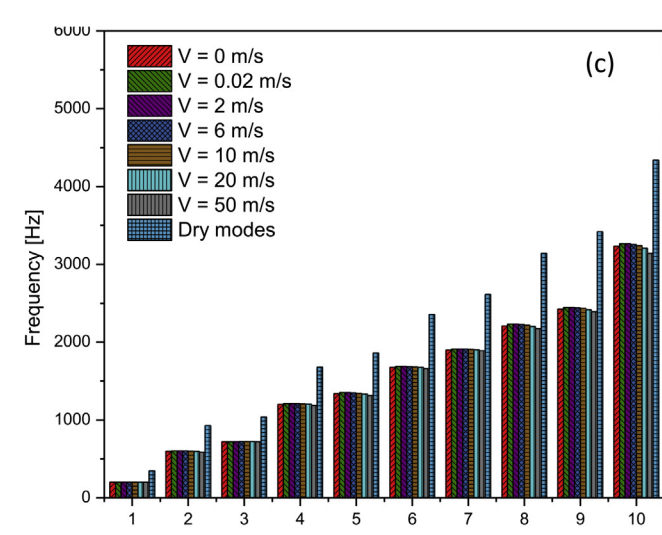
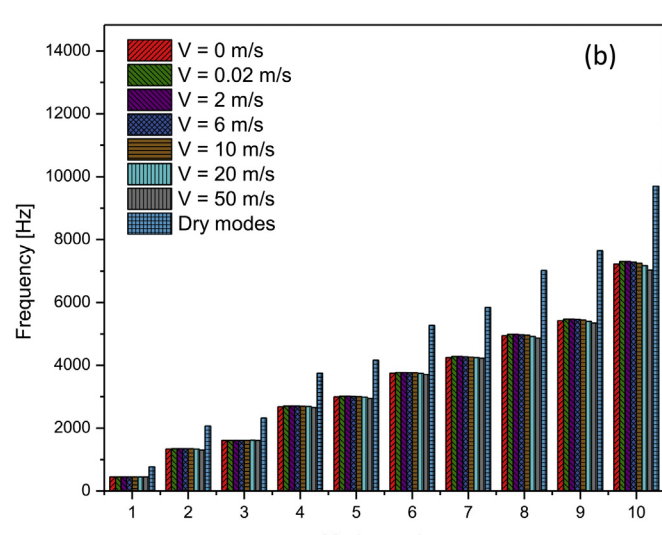
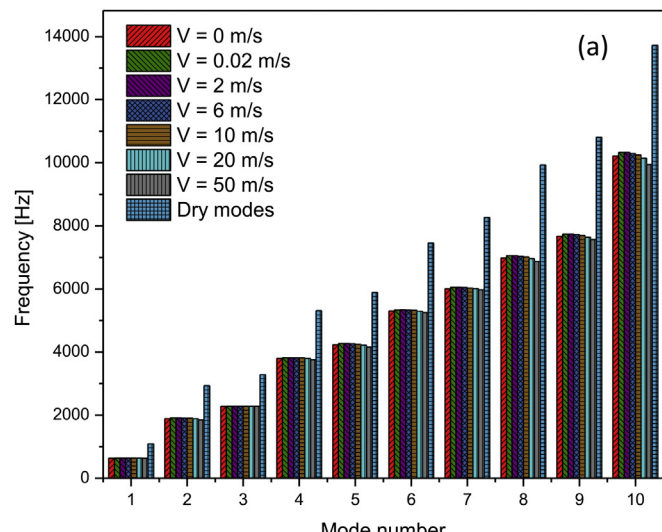


Fig. 10. Comparison of the first ten modes of propeller 4381 blade ($J = 0.8$, $f = 1300$ Hz): (a) $E = 210$ GPa; (b) $E = 105$ GPa; (c) $E = 21$ GPa.

Table 5

Comparison of added mass effect with various elastic modulus under advance ratio $J = 0.8$ and excitation frequency $f = 1300$ Hz.

Mode number	$(f_{air} - f_{water} _{V=0})/f_{air} \times 100$			$(f_{water} _{V=0} - f_{water} _{V=50})/f_{water} _{V=0} \times 100$		
	$E = 210\text{GPa}$	$E = 105\text{GPa}$	$E = 21\text{GPa}$	$E = 210\text{GPa}$	$E = 105\text{GPa}$	$E = 21\text{GPa}$
1	41.8	41.8	41.8	0.022	0.022	0.022
10	25.6	25.6	25.6	2.71	2.71	2.71

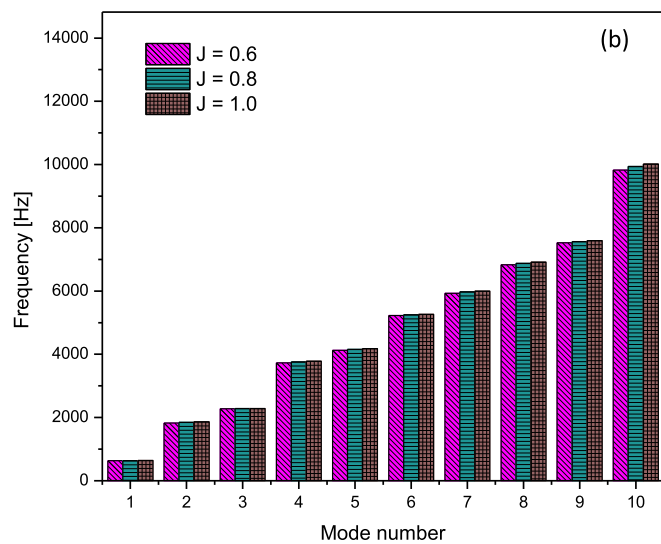
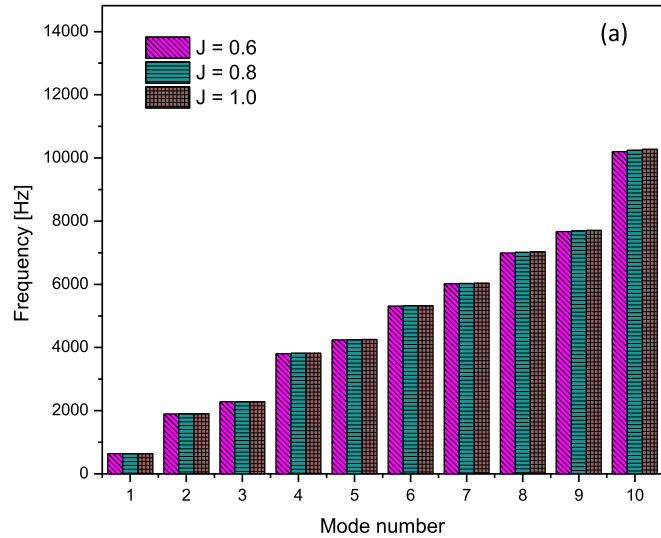


Fig. 11. Comparison of the first ten modes of propeller 4381 blade by different advance ratios ($E = 210\text{ GPa}$, $f = 1300$ Hz): (a) $V = 10\text{ m/s}$; (b) $V = 50\text{ m/s}$.

as: $J = 0.6, 0.8, 1.0$. It is observed from Fig. 11 that the natural frequencies increase as the advance ratio is increased. This is because an increase in the advance ratio leads to a decrease in the total incoming flow velocity, when the inflow velocity V is kept as constant.

4.2. The added damping characteristics

To demonstrate the effect of the added damping, the unsteady axial reactions of the same blade considered in Sec. 4.1.2 are calculated. However, in order to eliminate the influence of the added mass on unsteady axial reactions, only the added damping matrix is included in Eq. (23). The four propeller models in wet condition examined in Sec. 4.1.1 are considered here to analyze the terms generated by $((\delta \cdot \nabla) \mathbf{V}_0) \cdot \mathbf{n}$ and the imaginary part of the added damping. The comparison of the

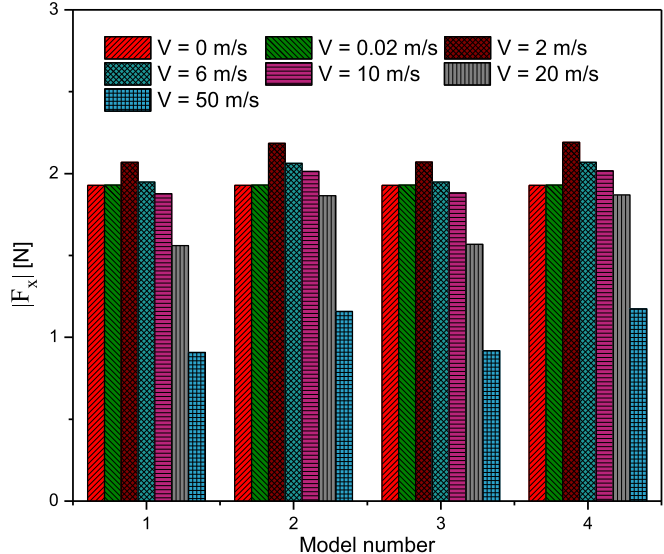


Fig. 12. Comparison of the unsteady axial forces of propeller 4381 blade under various inflow velocities ($J = 0.8$, $f = 1300$ Hz).

unsteady axial forces due to various inflow velocities is shown in Fig. 12. The advance ratio and the excitation frequency are taken as $J = 0.8$ and $f_0 = 1300$ Hz. For this case, the rotating speed of the propeller is obtained by the advance ratio. From the results, we can conclude:

- (1) The term of $((\delta \cdot \nabla) \mathbf{V}_0) \cdot \mathbf{n}$ can be neglected for formulating the added damping matrix. This indicates that the non-penetration boundary condition can be imposed on the undeformed blade surface for analyzing the effect of added damping. However, the

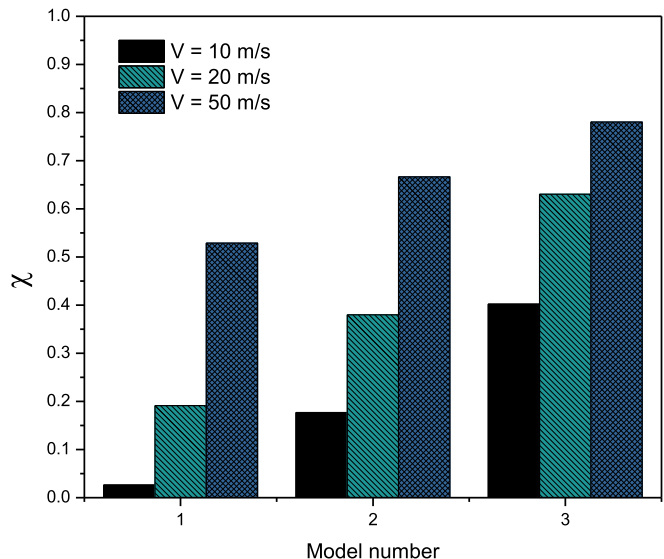


Fig. 13. Comparison of damping effect of propeller 4381 blade under various inflow velocities ($J = 0.8$). Model 1: $E = 210\text{ GPa}$, $f = 1300$ Hz. Model 2: $E = 105\text{ GPa}$, $f = 920$ Hz. Model 3: $E = 21\text{ GPa}$, $f = 410$ Hz.

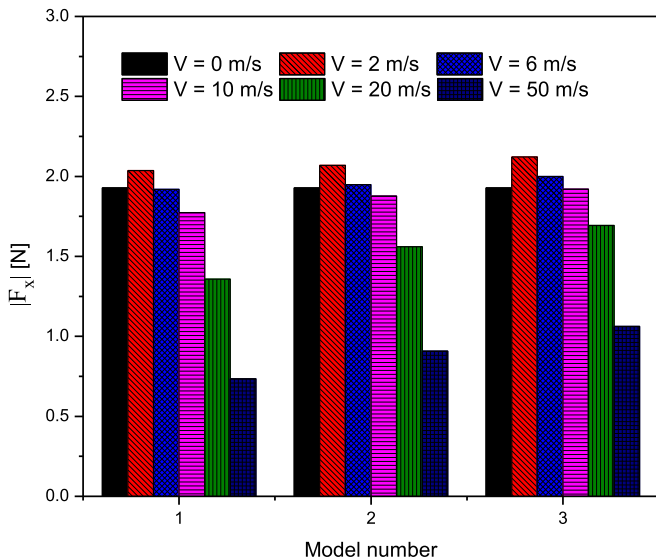


Fig. 14. Comparison of the unsteady axial forces of propeller 4381 blade under various inflow velocities ($E = 210 \text{ GPa}$, $f = 1300 \text{ Hz}$). Model 1: $J = 0.6$. Model 2: $J = 0.8$. Model 3: $J = 1.0$.

terms of the imaginary part are important, when the inflow velocity is relatively large.

- (2) As the inflow velocity is relatively large, the added damping will significantly affect the unsteady performance of the propeller. This is due to the fact that the term of \mathbf{V}_0^x exists in the formula of the added damping matrix.

Furthermore, the effect of the elastic modulus on the added damping is investigated, and the results are shown in Fig. 13. Considering the same propeller blade with the same trick described above, the relative reduction ratio $\chi (= (F_x(0) - F_x(V)) / F_x(0))$ of the unsteady axial reaction due to the added damping is calculated, where $F_x(V)$ is the axial reaction of the propeller subjected to inflow velocity V and $F_x(0)$ is the axial reaction for the propeller in stationary water. The added terms generated by $((\delta \nabla) \mathbf{V}_0) \cdot \mathbf{n} (D \neq 0)$, and the imaginary part of the added mass both are considered here (Model #1 in Fig. 12 is considered). The driving frequencies of the excitation forces are taken as 1300 Hz, 920 Hz, and 410 Hz. It is to note that the fundamental frequency of the propeller blade in dry condition is 1094 Hz, 774 Hz and 346 Hz when elastic modulus E is taken as 210 GPa, 105 GPa, and 21 GPa, respectively. Therefore, the ratio of the driving frequency to the fundamental frequency is almost constant in the three cases.

It is observed that the axial reaction is smaller as the inflow velocity is

Appendix A. Kinematic boundary conditions on blade surface

In Cartesian coordinate system as shown in Fig. 1, the material point (x, y, z) on the blade surface can be described as $(\delta^x(x, y, z, t), \delta^y(x, y, z, t), \delta^z(x, y, z, t))$. The position of the point becomes $(\bar{x}, \bar{y}, \bar{z})$, which is expressed:

$$(\bar{x}, \bar{y}, \bar{z}) = (x, y, z) + (\delta^x(x, y, z, t), \delta^y(x, y, z, t), \delta^z(x, y, z, t)) \quad (\text{A.1})$$

Let $n(x, y, z) = 0$ define geometrical function which describes the undeformed surface, and then the deformed surface equation can be written as:

$$N(\bar{x}, \bar{y}, \bar{z}) = n(\bar{x} - \delta^x, \bar{y} - \delta^y, \bar{z} - \delta^z) = 0 \quad (\text{A.2})$$

Supposing the normal vector of the deformed blade surface at point $(\bar{x}, \bar{y}, \bar{z})$ is $(N_{\bar{x}}, N_{\bar{y}}, N_{\bar{z}})$, then:

$$\begin{aligned} N_{\bar{x}} &= n_x \left(1 - \delta_x^x \bar{x}_{\bar{x}} - \delta_y^x \bar{y}_{\bar{x}} - \delta_z^x \bar{z}_{\bar{x}} \right) + n_y \left(-\delta_x^y \bar{x}_{\bar{x}} - \delta_y^y \bar{y}_{\bar{x}} - \delta_z^y \bar{z}_{\bar{x}} \right) + n_z \left(-\delta_x^z \bar{x}_{\bar{x}} - \delta_y^z \bar{y}_{\bar{x}} - \delta_z^z \bar{z}_{\bar{x}} \right) \\ N_{\bar{y}} &= n_x \left(-\delta_x^x \bar{x}_{\bar{y}} - \delta_y^x \bar{y}_{\bar{y}} - \delta_z^x \bar{z}_{\bar{y}} \right) + n_y \left(1 - \delta_x^y \bar{x}_{\bar{y}} - \delta_y^y \bar{y}_{\bar{y}} - \delta_z^y \bar{z}_{\bar{y}} \right) + n_z \left(-\delta_x^z \bar{x}_{\bar{y}} - \delta_y^z \bar{y}_{\bar{y}} - \delta_z^z \bar{z}_{\bar{y}} \right) \\ N_{\bar{z}} &= n_x \left(-\delta_x^x \bar{x}_{\bar{z}} - \delta_y^x \bar{y}_{\bar{z}} - \delta_z^x \bar{z}_{\bar{z}} \right) + n_y \left(-\delta_x^y \bar{x}_{\bar{z}} - \delta_y^y \bar{y}_{\bar{z}} - \delta_z^y \bar{z}_{\bar{z}} \right) + n_z \left(1 - \delta_x^z \bar{x}_{\bar{z}} - \delta_y^z \bar{y}_{\bar{z}} - \delta_z^z \bar{z}_{\bar{z}} \right) \end{aligned} \quad (\text{A.3})$$

where δ_x^x represents taking the x direction spatial derivative of δ^x , and $x_{\bar{x}}$ represents taking the \bar{x} direction spatial derivative of x . Other symbols are similar to the definition of δ_x^x and $x_{\bar{x}}$.

Taking the spatial derivative to both sides of Eq. (A.1), one can calculate $x_{\bar{x}}$ and so on:

$$\begin{bmatrix} 1 + \delta_x^x & \delta_y^x & \delta_z^x \\ \delta_x^y & 1 + \delta_y^y & \delta_z^y \\ \delta_x^z & \delta_y^z & 1 + \delta_z^z \end{bmatrix} \begin{bmatrix} x_{\bar{x}} & x_{\bar{y}} & x_{\bar{z}} \\ y_{\bar{x}} & y_{\bar{y}} & y_{\bar{z}} \\ z_{\bar{x}} & z_{\bar{y}} & z_{\bar{z}} \end{bmatrix} = \begin{bmatrix} 1 & 0 & 0 \\ 0 & 1 & 0 \\ 0 & 0 & 1 \end{bmatrix} \quad (\text{A.4})$$

Assuming the unknown displacement is small, and substituting Eq. (A.4) into Eq. (A.3) gives:

$$\begin{aligned} N_{\bar{x}} &= n_x - n_x \delta_x^x - n_y \delta_x^y - n_z \delta_x^z \\ N_{\bar{y}} &= n_y - n_x \delta_y^x - n_y \delta_y^y - n_z \delta_y^z \\ N_{\bar{z}} &= n_z - n_x \delta_z^x - n_y \delta_z^y - n_z \delta_z^z \end{aligned} \quad (\text{A.5})$$

The velocity component normal to the solid boundaries of the deformed blade must be zero:

$$\left(\mathbf{V}_0(\bar{x}, \bar{y}, \bar{z}, t) + \nabla \phi(\bar{x}, \bar{y}, \bar{z}, t) - \frac{\partial \boldsymbol{\delta}}{\partial t}(\bar{x}, \bar{y}, \bar{z}, t) \right) \cdot (N_{\bar{x}} \mathbf{i} + N_{\bar{y}} \mathbf{j} + N_{\bar{z}} \mathbf{k}) = 0 \quad (\text{A.6})$$

where $\mathbf{V}_0(\bar{x}, \bar{y}, \bar{z}, t)$ represents the velocity vector of uniform flow. $\nabla \phi(\bar{x}, \bar{y}, \bar{z}, t)$ represents the induced velocity generated by deformed blade. $\frac{\partial \boldsymbol{\delta}}{\partial t}(\bar{x}, \bar{y}, \bar{z}, t)$ represents the velocity vector of the point $(\bar{x}, \bar{y}, \bar{z})$. By applying Taylor's expansion for $\mathbf{V}_0(\bar{x}, \bar{y}, \bar{z}, t)$, $\nabla \phi(\bar{x}, \bar{y}, \bar{z}, t)$ and $\frac{\partial \boldsymbol{\delta}}{\partial t}(\bar{x}, \bar{y}, \bar{z}, t)$ gives:

$$\begin{aligned} \mathbf{V}_0(\bar{x}, \bar{y}, \bar{z}, t) &= \mathbf{V}_0(x, y, z, t) + (\boldsymbol{\delta} \cdot \nabla) \mathbf{V}_0(x, y, z, t) \\ \nabla \phi(\bar{x}, \bar{y}, \bar{z}, t) &= \nabla \phi(x, y, z, t) + (\boldsymbol{\delta} \cdot \nabla) \nabla \phi(x, y, z, t) \\ \frac{\partial \boldsymbol{\delta}}{\partial t}(\bar{x}, \bar{y}, \bar{z}, t) &= \frac{\partial \boldsymbol{\delta}}{\partial t}(x, y, z, t) + (\boldsymbol{\delta} \cdot \nabla) \frac{\partial \boldsymbol{\delta}}{\partial t}(x, y, z, t) \end{aligned} \quad (\text{A.7})$$

Assume $\nabla \phi(x, y, z, t)$ is small. Substituting Eq. (A.5) and Eq. (A.7) into Eq. (A.6) gives kinematic boundary condition on blade surface, written by:

$$\frac{\partial \boldsymbol{\delta}}{\partial t} \cdot \mathbf{n} = \frac{\partial \phi}{\partial \mathbf{n}} + \mathbf{V}_0 \cdot \mathbf{n} + ((\boldsymbol{\delta} \cdot \nabla) \mathbf{V}_0 - (\mathbf{V}_0 \cdot \nabla) \boldsymbol{\delta}) \cdot \mathbf{n} \quad (\text{A.8})$$

Here, \mathbf{n} is the unit normal vector of the undeformed blade surface at point (x, y, z) , and \mathbf{n} has the form: $\frac{1}{\sqrt{n_x^2 + n_y^2 + n_z^2}} (n_x, n_y, n_z)$.

As the blade is assumed to be of small elastic deformations, therefore we obtain $\|\nabla \boldsymbol{\delta}\| = o(\boldsymbol{\delta})$ and the following equation:

$$-\frac{\partial \phi}{\partial \mathbf{n}} \cong \mathbf{V}_0 \cdot \mathbf{n} - \frac{\partial \boldsymbol{\delta}}{\partial t} \cdot \mathbf{n} + ((\boldsymbol{\delta} \cdot \nabla) \mathbf{V}_0) \cdot \mathbf{n} \quad (\text{A.9})$$

For the sake of convenience, the boundary conditions by above equation can be further decomposed into two different boundary conditions, given as:

$$-\frac{\partial \phi_s}{\partial \mathbf{n}} = \mathbf{V}_0 \cdot \mathbf{n} \quad (\text{A.10})$$

$$-\frac{\partial \phi_v}{\partial \mathbf{n}} = -\frac{\partial \boldsymbol{\delta}}{\partial t} \cdot \mathbf{n} + ((\boldsymbol{\delta} \cdot \nabla) \mathbf{V}_0) \cdot \mathbf{n} \quad (\text{A.11})$$

where Eq. (A.10) and Eq. (A.11) are the kinematic boundary conditions for the rigid blade and elastic blade, respectively.

Appendix B. Comparisons between fluid-structure interaction and acoustic-solid interaction

In the view of the Cartesian coordinate system mentioned in Sec. 2.1, the sound pressure field $\tilde{p}(\mathbf{R}, t)$ is governed by a 3D wave equation $\nabla^2 \tilde{p}(\mathbf{R}, t) - \frac{1}{c_0^2} \frac{\partial^2 \tilde{p}(\mathbf{R}, t)}{\partial t^2} = 0$ in the time domain. Assuming $\tilde{p}(\mathbf{R}, t) = p(\mathbf{R}) e^{i\omega t}$, Helmholtz equation will be obtained as:

$$\nabla^2 p(\mathbf{R}) + k^2 p(\mathbf{R}) = 0 \quad (\text{B.1})$$

where, $k = \omega/c_0$, and c_0 is the speed of sound. In order to calculate the sound pressure amplitude $p(\mathbf{R})$ in Eq. (B.1), the following integral expression is employed:

$$2\pi p(\mathbf{R}_P) = \int_{S_B} p(\mathbf{R}_Q) \frac{\partial G(\mathbf{R}_P, \mathbf{R}_Q)}{\partial \mathbf{n}_Q} d\mathbf{s} - \int_{S_B} \frac{\partial p(\mathbf{R}_Q)}{\partial \mathbf{n}_Q} G(\mathbf{R}_P, \mathbf{R}_Q) d\mathbf{s} \quad (\text{B.2})$$

where, S_B denotes the blade surface. The subscript Q corresponds to the variable point in the integration, and the subscript P corresponds to the control

point on the panel. \mathbf{R}_P and \mathbf{R}_Q are the position vectors for points on the blade. $G(\mathbf{R}_P, \mathbf{R}_Q)$ is the Green's function for the Helmholtz equation in an unbounded 3-D fluid domain, which is given by $G(\mathbf{R}_P, \mathbf{R}_Q) = \frac{e^{-ik|\mathbf{R}_P - \mathbf{R}_Q|}}{|\mathbf{R}_P - \mathbf{R}_Q|}$. \mathbf{n}_Q is the outward unit normal vector. If and only if $k = 0$, the Green's function will be equal to that of the Laplace equation.

The kinematic boundary condition on the blade surface for the acoustic solid coupling system requires that normal velocity and acceleration on the blade are equal to those of fluid particle at the same position, which gives:

$$\nabla \tilde{p}(\mathbf{R}, t) = -\rho \frac{\partial \tilde{\mathbf{v}}(\mathbf{R}, t)}{\partial t} = -\rho \frac{\partial^2 \tilde{\delta}(\mathbf{R}, t)}{\partial t^2} \quad (\text{on blade surface } \Gamma) \quad (\text{B.3})$$

Eq. (B.3) could be rewritten as:

$$\frac{\partial \tilde{p}}{\partial \mathbf{n}} = -\rho \frac{\partial^2 \tilde{\delta}_n(\mathbf{R}, t)}{\partial t^2} \quad (\text{B.4})$$

After a mathematical analysis, supposing $\tilde{\delta}_n(\mathbf{R}, t) = \delta_n(\mathbf{R})e^{i\omega t}$ would be suitable and $\tilde{p}(\mathbf{R}, t) = p(\mathbf{R})e^{i\omega t}$, Eq. (B.4) could be expressed as:

$$\frac{\partial p}{\partial \mathbf{n}} = \rho \omega^2 \delta_n \quad (\text{B.5})$$

Substituting Eq. (B.5) back into Eq. (B.2), the discretized form of Eq. (B.2) can be written as follows:

$$\{p\} = -\rho \omega^2 \left(2\pi \mathbf{I} - \left[\frac{\partial G}{\partial \mathbf{n}} \right] \right)^{-1} \mathbf{G}\{\delta_n\} \quad (\text{B.6})$$

The nodal force vector is written as:

$$\mathbf{f} = \mathbf{Z}^T \Delta s \{p\} = -\rho \omega^2 \mathbf{Z}^T \Delta s \left(2\pi \mathbf{I} - \left[\frac{\partial G}{\partial \mathbf{n}} \right] \right)^{-1} \mathbf{G} \mathbf{Z} \mathbf{u} \quad (\text{B.7})$$

As $G(\mathbf{R}_P, \mathbf{R}_Q) = \frac{e^{-ik|\mathbf{R}_P - \mathbf{R}_Q|}}{|\mathbf{R}_P - \mathbf{R}_Q|} = \frac{\cos(k|\mathbf{R}_P - \mathbf{R}_Q|) - i \sin(k|\mathbf{R}_P - \mathbf{R}_Q|)}{|\mathbf{R}_P - \mathbf{R}_Q|}$, the nodal force could be rewritten as $\mathbf{f} = -(\mathbf{M}_a \mathbf{u} + i \mathbf{C}_a \mathbf{u})$, where \mathbf{M}_a and \mathbf{C}_a are the vector added-mass and added-damping matrices.

After a rigorous derivation, the following statement could be proven:

Only if $k = 0$, $\mathbf{M}_a = \mathbf{M}_w|_{V_0=0}, \mathbf{C}_a = \mathbf{C}_w|_{V_0=0} = \mathbf{0}$.

In summary, the add-mass matrix due to fluid-structure interaction in the stationary flow is equal to that from acoustic-solid interaction when wave number of sound is zero, and added-damping the added-damping matrix will vanish in this situation. Thus, the fluid-structure interaction governing equation will have the same solution as that of the acoustic-solid interaction governing equation.

References

- Gao, X.-W., 2005. Evaluation of regular and singular domain integrals with boundary-only discretization—theory and Fortran code. *J. Comput. Appl. Math.* 175, 265–290.
- Gaschler, M., Abdel-Maksoud, M., 2014. Computation of hydrodynamic mass and damping coefficients for a cavitating marine propeller flow using a panel method. *J. Fluids Struct.* 49, 574–593. <https://doi.org/10.1016/j.jfluidstructs.2014.06.001>
- Ghassemi, Hassan, Kohansal, A.R., 2009. Numerical evaluation of various levels of singular integrals, arising in BEM and its application in hydrofoil analysis. *Appl. Math. Comput.* 213, 277–289.
- Hess, J.L., Smith, A.M.O., 1967. Calculation of potential flow about arbitrary bodies. *Prog. Aeronaut. Sci.* 8, 1–138.
- Hess, J.L., Smith, A.M.O., 1964. Calculation of non-lifting potential flow about arbitrary three-dimensional bodies. *J. Sh. Res.* 8, 22–44.
- Lin, H.J., Tsai, J.F., 2008. Analysis of underwater free vibrations of a composite propeller blade. *J. Reinf. Plast. Compos.* 27, 447–458. <https://doi.org/10.1177/0731684407082539>.
- MacPherson, D.M., Puleo, V.R., Packard, M.B., 2007. Estimation of Entrained Water Added Mass Properties for Vibration Analysis. The Society of Naval Architects & Marine Engineers, New England Section.
- Mao, Y., Young, Y.L., 2016. Influence of skew on the added mass and damping characteristics of marine propellers. *Ocean. Eng.* 121, 437–452. <https://doi.org/10.1016/j.oceaneng.2016.05.046>.
- Martio, J., Sánchez-Caja, A., Siikonen, T., 2015. Evaluation of propeller virtual mass and damping coefficients by URANS- method. In: International Symposium on Marine Propulsors.
- Morino, L., Kuo, C.-C., 1974. Subsonic potential aerodynamic for complex configurations: a general theory. *AIAA J.* 12, 191–197.
- Parsons, M.G., Vorus, W.S., Richard, E.M., 1980. Added Mass and Damping of Vi-Brating Propellers. Technical Report. University of Michigan.
- Peters, H., Marburg, S., Kessissoglou, N., 2012. Structural-acoustic coupling on non-conforming meshes with quadratic shape functions. *Int. J. Numer. Methods Eng.* 91, 27–38.
- Schwanencke, H., 1963. Gedanken zur frage der hydrodynamischen erregungen des propellers und der wellenleitung. In: STG-Jahrbuch, Schiffbautechnische Gesellschaft e.V. (STG).
- Tarafder, M.S., Saha, G.K., Mehedi, S.T., 2010. Analysis of potential flow around 3-Dimensional hydrofoils by combined source and dipole based panel method. *J. Mar. Sci. Technol.* 18, 376–384.
- Tian, J., Croaker, P., Li, J., Hua, H., 2016. Experimental and numerical studies on the flow-induced vibration of propeller blades under nonuniform inflow. *Proc. Inst. Mech. Eng. Part M. J. Eng. Marit. Environ.* 231 <https://doi.org/10.1177/1475090216654306>.
- Tian, J., Zhang, Z., Ni, Z., Hua, H., 2017. Flow-induced vibration analysis of elastic propellers in a cyclic inflow: an experimental and numerical study. *Appl. Ocean. Res.* 65, 47–59. <https://doi.org/10.1016/j.apor.2017.03.014>.
- Yari, E., Ghassemi, H., 2016. Boundary element method applied to added mass coefficient calculation of the skewed marine. *Pol. Marit. Res.* 23, 25–31.
- Young, Y.L., 2007. Time-dependent hydroelastic analysis of cavitating propulsors. *J. Fluids Struct.* 23, 269–295. <https://doi.org/10.1016/j.jfluidstructs.2006.09.003>.